ACCSCIENCE PUBLISHING

Journal of Seismic Exploration

ARTICLE

Geological survey and rock-physics seismic interpretation of an ultra-shallow gas reservoir in the deep-water Qiongdongnan Basin, China

Jianxiang Pei, Wanyuan Sun*, Fang Li, Yanhua Xie, Chongyan Wu, and Jinpeng Li

Research Institute, CNOOC Hainan Branch, Haikou, Hainan, China

Abstract

Ultra-shallow gas and hydrate-bearing systems in deep-water Quaternary strata are important exploration targets, but their geological controls and seismic responses remain difficult to quantify because the reservoirs are weakly consolidated, laterally heterogeneous, and commonly occur near the base of the gas-hydrate stability zone. This study presents an integrated geological and rock-physics seismic interpretation of the Lingshui 36-1 (LS36-1) ultra-shallow gas reservoir in the Qiongdongnan Basin. Regional geology, seismic interpretation, gas-source geochemistry, drilled sediment samples, and rock-physics modeling were combined into a case-specific interpretation workflow. The results indicate that shallow gas enrichment is controlled by the coupling of a Quaternary submarine-fan sand body, a fault-gas chimney-microfracture migration system, and three sealing elements: deep-water mud, mass-transport deposits, and hydrate-bearing intervals. The gas is methane-dominated dry gas related to mature to over-mature coal-measure source rocks of the Paleogene Yacheng Formation. Samples showed that the reservoirs are very weakly consolidated and highly porous; Ledong submarine-fan sandstone had porosities of 38.4%–42.5% and permeabilities of 48.4–598.4 mD, whereas a broader shallow-reservoir sample set showed porosities of 28.4%–43.6%. Laboratory velocity measurements were interpreted as trend-calibration data rather than pressure-equivalent reservoir velocities. In free-gas-bearing samples, replacing gas with water increased P- and S-wave velocities; in hydrate-bearing samples, decreasing water saturation increased hydrate saturation and therefore increased stiffness. A Hertz–Mindlin–Hashin–Shtrikman–Gassmann workflow, constrained by well logs and calibrated mineral/fluid parameters, predicted high P-wave impedance at the top of hydrate-bearing intervals and low P-wave impedance at the top of free-gas intervals. We therefore used P-wave impedance to identify sand-prone reservoirs, while the P-wave velocity ratio ranked high gas-saturation intervals. The inversion is consistent with LS36-1 well data but lacks independent blind-well validation because no additional verification well is available. The workflow provides a case-specific, uncertainty-aware approach for evaluating deep-water ultra-shallow gas and hydrate-associated reservoirs.

Keywords: Quaternary seabed; Ultra-shallow gas reservoir; Lingshui 36-1; Qiongdongnan Basin; Gas-hydrate stability; Rock physics; Seismic inversion

***Corresponding author:**
Wanyuan Sun
(sunwy5@cnooc.com.cn)

Citation: Pei J, Sun W, Li F, Xie Y, Wu C, Li J. Geological survey and rock-physics seismic interpretation of an ultra-shallow gas reservoir in the deep-water Qiongdongnan Basin, China. *J Seismic Explor.* doi: 10.36922/JSE026210088

Received: May 19, 2026

Revised: September 8, 2026

Accepted: September 8, 2026

Published online: November 5, 2026

Copyright: © 2026 Author(s). This is an Open-Access article distributed under the terms of the Creative Commons Attribution License, permitting distribution, and reproduction in any medium, provided the original work is properly cited.

Publisher's Note: AccScience Publishing remains neutral with regard to jurisdictional claims in published maps and institutional affiliations.

1. Introduction

Distinguishing free gas from gas hydrate in ultra-deep-water, ultra-shallow Quaternary sediments is difficult because the two phases produce similar seismic amplitude anomalies but respond differently to pressure, temperature, and gas composition.[1] The term *ultra-shallow gas* is used here to refer to gas trapped in strata less than 300 m below the seabed in water depths exceeding 1,500 m. These shallow gas accumulations differ from conventional deep natural gas in three critical ways: they are mechanically weak and unconsolidated; they commonly coexist with gas hydrates under low-temperature and high-pressure conditions; and their seismic responses are strongly affected by both pore fluid and frame stiffness. In many deep-water basins, shallow gas was historically treated as a drilling hazard rather than a resource because resource density was considered low and exploration risks were poorly constrained.[2-4] Recent advances in high-resolution 3D seismic, seabed sampling, and rock-physics modeling have made it possible to evaluate these shallow targets with greater confidence.[5] If gas hydrate and free gas can be distinguished seismically, then shallow-gas production could potentially depressurize hydrate-bearing intervals and provide a new pathway for hydrate exploitation.[6-12]

This study focuses on the Lingshui 36-1 (LS36-1) accumulation in the Qiongdongnan Basin, northern South China Sea. For clarity, L36 is the exploration shorthand for LS36-1, whereas L18 denotes the adjacent LS18-1 area (Figure 1A, B). The Quaternary Ledong Formation in this area contains submarine-fan sand bodies, which are the main exploration targets for the ultra-shallow interval. The Qiongdongnan Basin is a Cenozoic passive continental-margin fault basin that developed through Paleogene rifting followed by Neogene-Quaternary thermal subsidence, resulting in a lower faulted system and an upper depression system.[13-16] Globally, gas hydrate has been identified in various deep-water settings, providing important analogs for the Qiongdongnan Basin.[17,18] Recent CNOOC exploration has confirmed the coexistence of shallow free gas, gas hydrate, and hydrate-related fluid flow in this area;[19-22] the gas is methane-dominated and genetically related to mature to over-mature coal-measure source rocks of the Paleogene Yacheng Formation.[23,24] Previous studies have also investigated the sedimentary characteristics and reservoir formation conditions of shallow gas in the Qiongdongnan Basin.[25] However, most previous work has described regional accumulation conditions, hydrate occurrence, or seismic anomalies separately; few have attempted to integrate gas-source geochemistry, laboratory velocity measurements, and rock-physics modeling into a single interpretation workflow for distinguishing free gas and hydrate in the ultra-shallow interval.[26-32] This is the first study to integrate gas-source geochemistry, laboratory velocity measurements, and rock-physics modeling into a unified interpretation workflow to distinguish free gas from hydrate in the ultra-shallow interval of the Qiongdongnan Basin.

The central research question of this paper is: when pressure–temperature conditions, gas migration, and seismic resolution all vary across a short vertical interval, how can free gas be distinguished from gas hydrate in weakly consolidated Quaternary sand bodies using conventional seismic data, and how can the seismic inversion be calibrated with limited well control? To address this, the study makes four case-specific contributions: (i) it links the Quaternary Ledong submarine-fan reservoir to the Yacheng coal-measure source and the fault-gas-chimney migration system; (ii) it calibrates a weakly consolidated sediment rock-physics model using X-ray diffraction (XRD), recovered samples, and LS3 well logs; (iii) it establishes a P-wave impedance and P-wave velocity ratio workflow for separating sand-prone, water-bearing and free-gas-bearing intervals, with hydrate-treated as a separate phase whose identification is primarily constrained by the gas-hydrate stability zone; and (iv) it applies the workflow to LS36-1 and explicitly acknowledges that the result is a single-well internal consistency check, not an independent validation; the interpretation is therefore presented as a feasibility study for target ranking pending future drilling verification.

2. Regional geological setting

The Qiongdongnan Basin is situated in the northern South China Sea and developed as a Cenozoic passive continental-margin fault basin (Figure 1A). It is bordered by the Yinggehai Basin to the southwest along the No. 1 fault zone, the Shenhu uplift and Zhusan sag to the northeast, the Hainan uplift to the northwest, and the Yongle uplift to the southeast, covering approximately 8×10^4 km^2. Water depths range from 80 to 3,500 m, with the deep-water area (depth > 300 m) covering approximately 5×10^4 km^2. The maximum water depth exceeds 3,000 m in the southern part, and Cenozoic sedimentary successions locally exceed 10 km in thickness. From northwest to southeast, the first-order tectonic units consist of the northern depression, central uplift, central depression, and southern uplift belts, which can be further subdivided into secondary structural units, including the Lingshui sag, Beijiao sag, and Lingnan low uplift (Figure 1B).

The LS36-1 gas field is located in the Songnan-Lingshui deep-water area and contains two reservoir-seal assemblages in the second and third members of the

Quaternary Ledong Formation. The reservoir lithology is dominated by siltstone and muddy siltstone, with minor fine- to medium-grained sand. Figure 2 shows examples of seabed gas leakage and recovered hydrate-bearing samples from the Songnan low uplift area, indicating the presence of an active shallow gas system in this area. Sections 3–5 conduct rock-physics modeling and seismic interpretation based on the geological background described above.

Exploration practice indicates that ultra-shallow gas in the Qiongdongnan Basin occurs in two related but

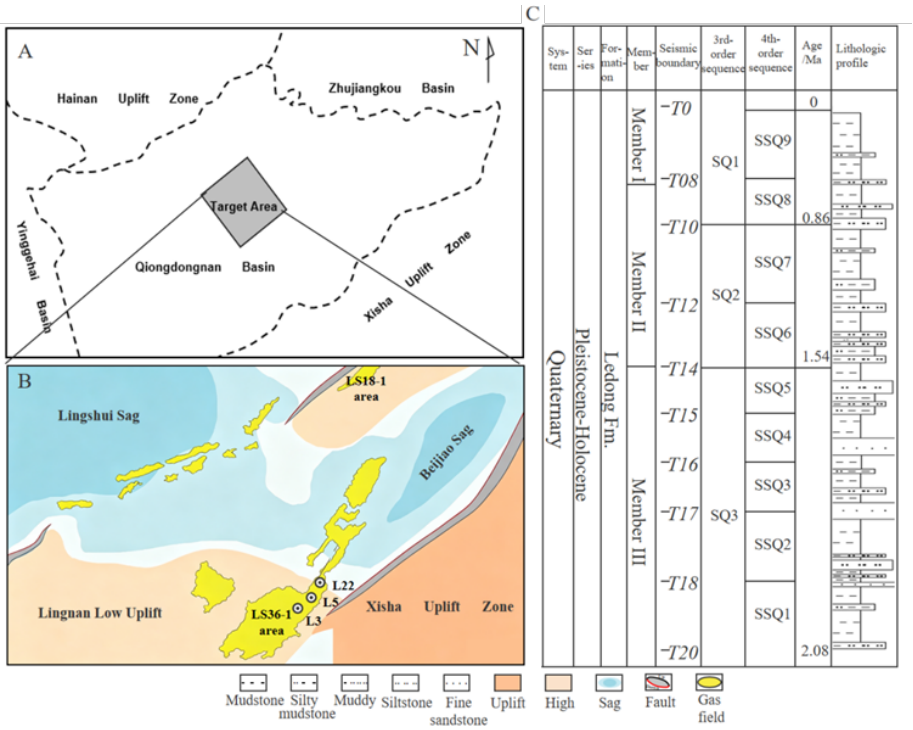


Figure 1. Qiongdongnan Basin location, local structural setting, and Quaternary stratigraphic framework. (A) Location of the Lingshui 36-1 (LS36-1) gas field in the target area. (B) Tectonic map of the Qiongdongnan Basin, with boundaries of major second-order tectonic units, locations of key wells, and schematic extent of 2D/3D seismic coverage. (C) Composite stratigraphic column of the Ledong Formation in the Qiongdongnan Basin, showing member subdivision, dominant lithologies, thickness ranges, and seismic reflection characteristics.

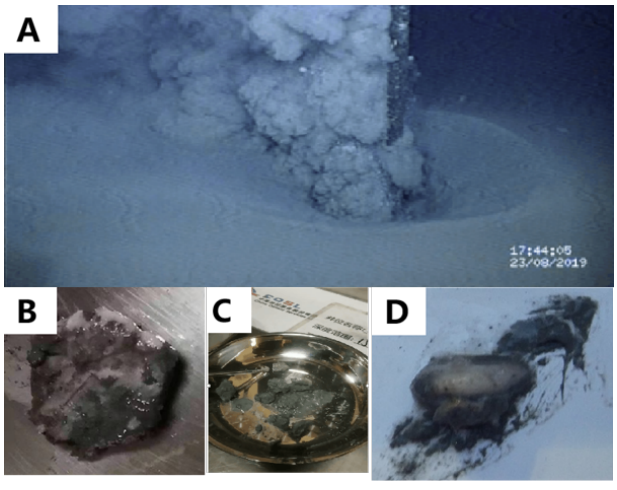


Figure 2. Examples of seabed shallow-gas leakage and hydrate-bearing samples from exploration wells in the Songnan low uplift area: (A) seabed gas leakage; (B–D) recovered hydrate-bearing samples.

physically distinct phases: free gas and gas hydrate. Phase state depends primarily on pressure, temperature, and gas composition. For reproducibility, the stability sensitivity was expressed with the relations:

$$P = 10.1 \times H \text{ (MPa, with } H \text{ in km)} \quad (1)$$

for hydrostatic pressure at water depth H;

$$T = T_b + Gz \text{ (with } z \text{ in km)} \quad (2)$$

for temperature below the seabed; and:

$$P = P_eq(T, x_CH_4) \quad (3)$$

for the methane-hydrate phase boundary. Here, T_b is the assumed seabed temperature (4 °C as the nominal case, with a ±1 °C sensitivity), G is the geothermal gradient, and P_eq is the equilibrium pressure corresponding to gas composition x_CH_4. The calculations used methane-dominated end members with x_CH_4 of 0.95–0.98 and minor C2+ components; the two gas end members plotted in Figure 3 correspond to relative gas-density values of 0.56 and 0.60. The geothermal-gradient scenarios are 60, 85, 100, and 110 °C/km. The family of curves in Figure 3 is therefore an uncertainty envelope: 60 °C/km represents the background case, 85 °C/km an intermediate case, and 100–110 °C/km high-fluid-flow cases. Under the nominal assumptions, the approximate minimum water depths for biogenic methane hydrate and mature thermogenic methane hydrate are 334 m and 548 m, respectively. These are model-based central estimates, not measured boundaries; uncertainty increases with lateral heat-flow, seabed-temperature, and gas-composition variation. The phase equilibrium calculations follow the Sloan model and were implemented in the CSMHYD program (Colorado School of Mines, United States of America) to calculate the methane hydrate pressure-temperature boundary.

3. Data, methods, and geological framework

3.1. Dataset and study scope

The dataset integrated regional geological framework data with a quantitative case study of the LS36-1 field. Available data included regional 2D and 3D seismic profiles, together with post-stack and pre-stack seismic volumes; well-log data from the LS3 well (L3 in Figure 1B), comprising gamma ray, resistivity, sonic (P-wave and S-wave velocity), bulk density, and neutron porosity logs, with a sampling interval of 0.125 m over the logged interval of 400–650 m below seafloor; 30 drill-cutting samples for XRD analysis (Table 1), distributed at approximately 8 m spacing across 404–640 m depth; 4 recovered core samples (1.40–78.35 m below seafloor), with diameters of 50–70 mm and lengths of 100–200 mm, used for direct velocity measurements (Table 2); 25 artificial rock-physics analogs with documented grain size, mineral content, and porosity (Table 3), prepared by mixing mineral powders and quartz sands with controlled grain sizes and loosely loaded into

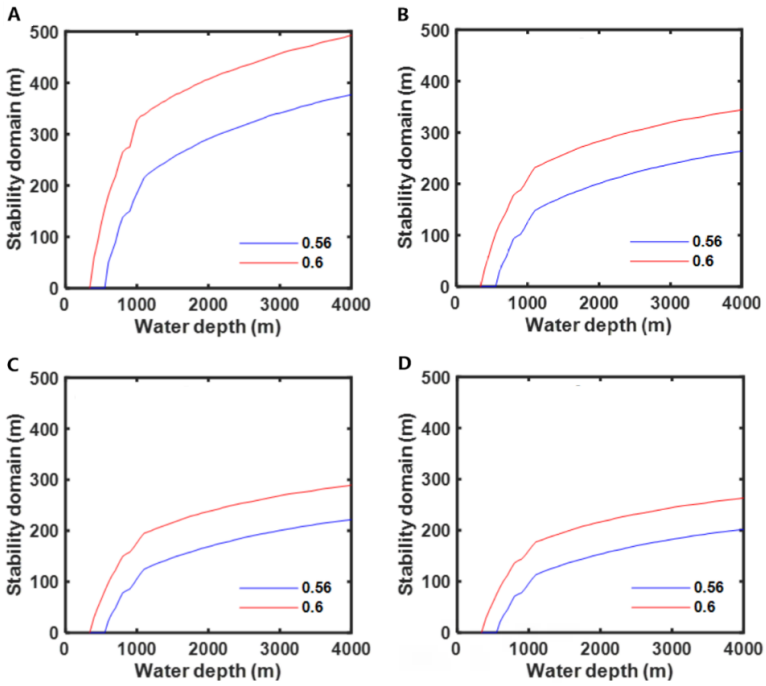


Figure 3. Hydrate-stability sensitivity for geothermal gradients of (A) 60, (B) 85, (C) 100, and (D) 110 °C/km

Table 1. X-ray diffraction mineral composition of drilled cuttings from the Lingshui 36-1 target area

Number	Depth (m)	Non-clay mineral content (%)							Clay (%)
		Quartz	Potassium feldspar	Plagioclase feldspar	Calcite	Fe-dolomite	Siderite	Halite	
1	404	39	3	15	8	4	1	1	29
2	412	39	4	17	7	4	1	1	27
3	420	41	4	13	6	2	1	1	32
4	424	42	7	17	8	2	1	1	22
5	428	45	3	15	6	3	2	1	25
6	432	49	2	19	7	2	–	1	20
7	620	47	1	22	9	–	–	2	19
8	624	50	5	15	10	1	–	1	18
9	632	49	5	9	6	1	1	1	28
10	640	47	10	12	6	1	–	1	23
11	404	37	4	14	6	5	1	2	31
12	412	41	5	14	6	3	1	2	28
13	420	41	5	18	6	–	1	3	26
14	424	41	7	19	6	–	1	2	24
15	428	51	2	12	5	–	1	2	27
16	432	43	3	15	7	3	1	3	25
17	624	45	8	19	5	–	1	1	21
18	628	47	6	13	5	3	1	2	23
19	636	50	2	12	6	4	1	2	23
20	640	39	9	18	5	5	1	2	21
21	404	41	3	17	4	1	1	1	32
22	412	39	6	13	6	4	1	2	29
23	420	43	7	17	6	1	1	2	23
24	424	50	6	17	7	3	–	1	16
25	428	47	6	19	5	3	–	1	19
26	432	49	7	14	6	3	1	1	19
27	608	46	13	13	5	4	–	1	18
28	612	50	5	15	5	6	–	1	18
29	616	44	13	17	4	2	–	1	19
30	620	50	9	14	5	2	–	1	19

polytetrafluoroethylene (PTFE) sleeves, yielding porosities ranging from 25.12% to 43.63%; gas composition and carbon isotope data; and published basin-scale geological constraints. Seismic data covered an area of approximately 320 km^2, with a dominant frequency of 30–45 Hz, a sampling rate of 1 ms, a trace spacing of 12.5 m × 12.5 m, and 60-fold coverage. The target interpretation interval was 140–700 ms two-way time below seafloor, and the pre-stack seismic volume included angle-stack information suitable for pre-stack inversion.

3.2. Workflow

The workflow consists of five steps: (i) mapping the Quaternary Ledong submarine-fan reservoir and associated mass-transport deposits from seismic facies; (ii) evaluating hydrocarbon supply from Yacheng Formation coal-measure source rocks using gas composition and carbon isotopes; (iii) constraining the hydrate stability domain from pressure–temperature–gas-composition assumptions; (iv) measuring and modeling elastic

Table 2. Laboratory velocity measurements of recovered samples from the Lingshui 36-1 target area

Sample	Depth (m)	Mineral content (%)							Vp (m/s)	Vs (m/s)
		Clay	Salt	Quartz	Potassium feldspar	Plagioclase feldspar	Calcite	Dolomite		
1	1.4–1.6	42.1	2.0	31.4	4.7	5.6	14.3	0	786	610
2	3.4–3.7	30.2	0.9	23.5	29.2	4.7	11.5	0	809	719
3	74.35	33.1	0	38.9	4.3	13.3	7	3.4	785	622
4	78.35	41.0	0	33.6	3.2	11.4	7.6	3.1	827	423

Table 3. Artificial samples prepared for velocity measurement experiments

Sample	Quartz (%)	Sodium feldspar (%)	Illite (%)	Chlorite (%)	Calcite (%)	Porosity (%)	Experiment type	Number
1	100 (150 μm)	–	–	–	–	40.18	Hydrate	S1
2	100 (1,000 μm)	–	–	–	–	42.56	Hydrate	S2
3	100 (75 μm)	–	–	–	–	38.89	Hydrate	S3
4	100 (150 μm)	–	–	–	–	41.74	Free gas	G1
5	70 (100 μm) +30 (62 μm)	–	–	–	–	27.71	Free gas	G2
6	59 (80 μm)	12	10	10	9	41.07	Free gas	G3
7	50 (500 μm)	20	–	20	10	27.71	Free gas	G4
8	90 (500 μm)	–	–	10	–	25.12	Free gas	G5
9	90 (500 μm)	–	–	10	–	31.84	Hydrate	S4
10	80 (100 μm) + 20 (38 μm)	–	–	–	–	29.76	Hydrate	S5
11	75 (500 μm)	–	–	25	–	30.89	Free gas	G6
12	75 (500 μm)	–	–	25	–	30.89	Hydrate	S6
13	41 (150 μm)	23	26	–	10	39.25	Free gas	G7
14	41 (150 μm)	23	26	–	10	36.52	Hydrate	S7
15	41 (150 μm)	26	24	–	9	35.84	Hydrate	S8
16	51 (150 μm)	14	27	–	8	37.81	Hydrate	S9
17	75 (50 μm)	–	–	25	–	38.80	Free gas	G8
18	75 (50 μm)	–	–	25	–	36.12	Free gas	G9
19	75 (50 μm)	–	–	25	–	43.63	Free gas	G10
20	75 (50 μm)	–	–	25	–	41.44	Free gas	G11
21	60 (150 μm)	5	27	–	8	36.27	Hydrate	S10
22	100 (500 μm)	–	–	–	–	32.16	Hydrate	S11
23	100 (500 μm)	–	–	–	–	39.73	Hydrate	S12
24	64 (150 μm)	–	26	–	10	40.83	Free gas	G12
25	100 (500 μm)	–	–	–	–	30.18	Free gas	G13

responses of weakly consolidated sediments and artificial samples; and (v) applying pre-stack inversion to predict P-wave impedance and P-wave velocity ratio, then converting these elastic indicators to porosity and free-gas saturation with the LS3-calibrated rock-physics template. For free-gas-bearing intervals, gas saturation is defined as:

$$Sg = 1 - Sw \quad (4)$$

Hydrate-bearing intervals are interpreted as a separate phase and were not forced into the free-gas saturation equation. Model predictions were checked against LS3 well information, but this check is described as internal consistency verification rather than independent blind validation.

3.3. Geological framework and accumulation model

The Qiongdongnan Basin developed through Paleogene continental rifting followed by Neogene-Quaternary marine thermal subsidence, producing a lower faulted system and an upper depression system. The central depression zone lies in the deep-water continental slope and contains Eocene lacustrine strata, Oligocene Yacheng Formation coal-measure and marginal-marine source rocks, and Miocene to Quaternary marine strata, including the Sanya, Meishan, Huangliu, and Ledong formations. The most important gas source for LS36-1 is interpreted as the Yacheng Formation coal-measure system, where humic organic matter reached mature to over-mature dry-gas generation stages.

Shallow gas accumulation conditions in the LS36-1 area are favorable because the source, migration, reservoir, and seal elements overlap spatially. Deep faults, gas chimneys, and shallow fractures connect mature Paleogene source rocks with Quaternary sand-rich deposits. In seismic interpretation, submarine-fan deposits are recognized by lobate to sheet-like, laterally continuous or moderately continuous reflections; sandy channels by confined, sinuous or erosional geometries with locally stronger amplitudes; mass-transport deposits by chaotic to transparent, discontinuous reflection packages; muddy background slope deposits by relatively continuous low-amplitude reflections; and delta-related deposits by progradational clinoforms outside the deep-water fan system. These criteria were used with amplitude and continuity rather than by amplitude alone. Petroleum-system terminology, including gas accumulation and hydrocarbon accumulation, was used consistently here. The most recent drilling and heat-flow constraints indicate an average geothermal gradient of approximately 60 °C/km, with local high-fluid-flow zones reaching 100–110 °C/km. These thermal variations directly affect hydrate stability and the vertical transition from hydrate-bearing intervals to free-gas intervals. The stratigraphic and structural framework of this accumulation model is summarized in Figure 4.

The Quaternary Ledong submarine fan is the principal shallow reservoir unit in the LS36-1 area. It develops mainly in the lower Ledong Formation and is expressed on seismic data as high-amplitude, laterally continuous to moderately continuous reflections. The minimum-amplitude attribute in Figure 5 delineates the main fan bodies and their relationship with adjacent delta-related deposits. Internally, the fan system includes distributary sandy channels, sheet-like fan deposits, local channel erosion, and muddy channel-abandonment fills. Mass-transport deposits and deep-water muds may act as local seals or baffles, whereas deltaic deposits occur outside the main deep-water fan system and should not be confused with the submarine-fan reservoir. Available sample statistics indicate that Ledong fan sandstones are mainly medium- to fine-grained sandstones. The sandstone subset has porosities of 38.4%–42.5% (average 40.5%) and permeabilities of 48.4–598.4 mD (average 312.2 mD), whereas the broader weakly consolidated shallow-reservoir sample set covers a wider porosity range of 28.4%–43.6%.

4. Gas-source geochemistry

The gas-source interpretation constrains hydrocarbon supply for the LS36-1 shallow accumulation rather than repeating a regional geochemical review. Shallow mudstones of the Ledong and Yinggehai formations locally reach poor to fair source-rock levels, as summarized using the hydrocarbon-generation and organic-matter diagrams in Figures 6 and 7. However, detailed gas-source correlation indicates that gas in LS36-1 is genetically related mainly to the Paleogene Yacheng Formation in the deeper Lingshui sag. The Yacheng Formation was deposited in a marine-continental transitional setting rich in terrestrial plant debris. During deep burial and thermal evolution, humic organic matter generated methane-dominated dry gas. The carbon isotope evidence does not support a dominant contribution from marine sapropelic type I/II organic matter.

Natural-gas composition and carbon isotopes indicate a mature to over-mature coal-type dry gas (Figure 8). Methane contents commonly exceed 95%, with only minor C2+ hydrocarbons. The relatively heavy methane and ethane carbon isotopic values are consistent with a humic gas source. The accumulation process is therefore interpreted as follows: gas generated from Yacheng Formation coal-measure source rocks migrated upward along deep faults, gas chimneys, and permeable transport layers and accumulated in Quaternary to Neogene

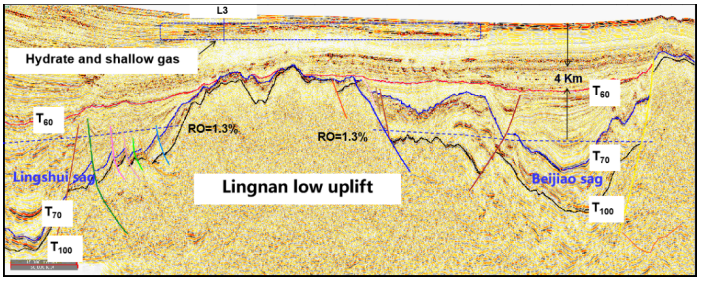


Figure 4. Stratigraphic and structural framework of the Lingshui 36-1 target area, showing the relationship between deep source rocks, migration pathways, Quaternary Ledong submarine-fan reservoirs, and shallow sealing intervals
Note: RO: Vitrinite reflectance; RO = 1.3% indicates a mature to high-mature source-rock interval.

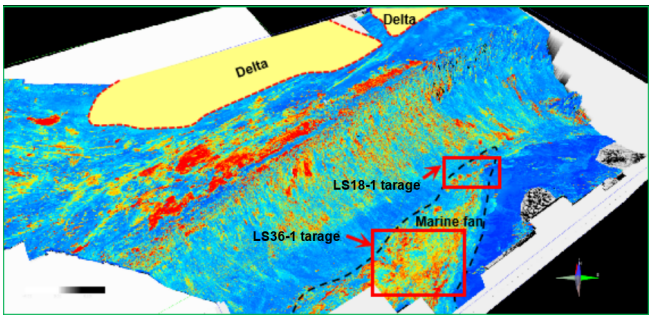


Figure 5. Minimum-amplitude attribute of post-stack seismic data within 140–700 ms below the seabed. Red rectangles indicate target areas; black dotted outlines indicate submarine-fan bodies; red dotted outlines indicate delta-related deposits.

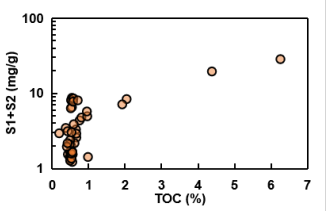


Figure 6. Hydrocarbon-generation potential of shallow source rocks in the Ledong and Yinggehai Formations. The figure provides regional context; the interpreted gas source for Lingshui 36-1 is mainly the deeper Yacheng coal-measure source system.
Abbreviation: TOC: Total organic carbon.

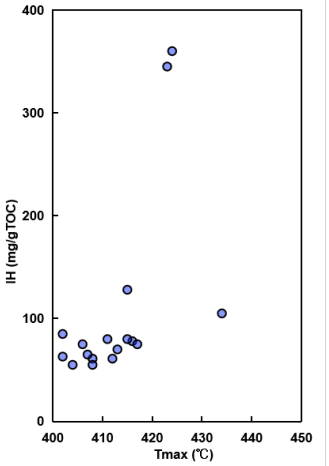


Figure 7. Organic-matter type diagram of shallow source rocks. The figure supports the distinction between shallow source potential and the deeper coal-measure gas source inferred for Lingshui 36-1.
Abbreviations: IH: Hydrogen index (mg HC/g TOC); TOC: Total organic carbon.

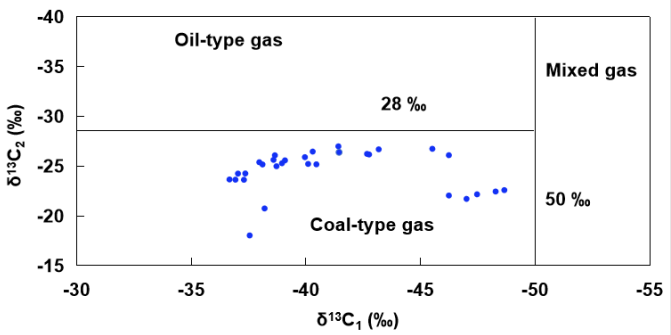


Figure 8. Gas-genesis discrimination based on methane and ethane carbon isotopes from the Lingshui sag and Lingshui 36-1-related gases. The panels distinguish coal-type thermogenic gas from biogenic and oil-associated gas trends.

submarine-fan sandstones where local hydrate-bearing intervals, mass-transport deposits, and deep-water muds provided sealing or baffling capacity.

The novelty of the geochemical section is its integration with the shallow seismic and rock-physics interpretation. Rather than presenting gas composition alone, the geochemical constraints define the source and migration end member required for hydrate/free-gas coexistence in the ultra-shallow reservoir system. This distinction also limits the interpretation: the available geochemical data support a coal-measure thermogenic source for LS36-1.

5. Rock physics and seismic interpretation

5.1. Rock-physics evidence from drilling

Sediment and cutting samples from the target area show a weakly consolidated, high-porosity and high-permeability reservoir system (Figures 9 and 10). The reservoir differs from conventional compacted sandstone because shallow burial, high pore pressure, loose grain contacts, and possible hydrate/free-gas coexistence jointly control its elastic response. The lithology is dominated by siltstone to fine sandstone. The drilled shallow-reservoir sample set has porosities of 28.4%–43.6%, whereas the Ledong fan sandstone subset has porosities of 38.4%–42.5% and permeabilities of 48.4–598.4 mD. These values explain why the reservoir can show low density and low velocity despite being sand-rich.

The XRD results from drilled cuttings showed that the shallow target interval is dominated by quartz, feldspar, and clay minerals. In Table 1, the mineral categories are mutually exclusive XRD groups; a "–" indicates below-detection or not detected, and row totals are normalized to 100%. Across 30 samples, quartz ranges from 37% to 51% (average 44.7%), K-feldspar from 1% to 13% (average 5.7%), plagioclase from 9% to 22% (average 15.5%), calcite from 4% to 10% (average 6.1%), Fe-dolomite from 1% to 6% where present, halite from 1% to 3%, and clay minerals from 16% to 32% (average 23.5%). This classification avoids overlap among quartz, feldspar, carbonate, and clay descriptions.

The mineralogical data showed a quartz-feldspar framework with significant clay content, consistent with weakly consolidated silty to fine-sandy submarine-fan deposits. These mineral proportions were used to constrain the Voigt–Reuss–Hill matrix moduli in the rock-physics model and to prepare representative artificial samples.

Four seabed or shallow subsurface sediment samples were selected for direct velocity measurement (Table 2; Figure 11). Samples 1 and 2 were shallow, high-water-content, paste-like sediments and were packed into vented PTFE sleeves for acoustic measurement. Samples 3 and 4 were deeper and more coherent, and were cut into regular cylindrical plugs. The measurements were laboratory measurements on recovered samples and therefore represent elastic-property trends and low-stress end members rather than *in situ* pressure–temperature velocities. This limitation is considered when comparing the experimental results with seismic and logging data.

The recovered sediment samples showed very low laboratory velocities, with P-wave velocities below 850 m/s and S-wave velocities below 750 m/s. These values are lower than seawater P-wave velocity, indicating extremely weak grain contacts under laboratory conditions. The result does not imply that *in situ* reservoir velocity is always below 1,500 m/s; rather, it explains why acoustic logging in very loose shallow formations can be unstable and why seismic inversion must be calibrated with a rock-physics model that accounts for stress, porosity, gas, and hydrate effects.

5.2. Artificial-sample experiments

Artificial samples were prepared according to the mineral compositions and porosity ranges observed in the drilled samples (Table 3). Mineral powders and quartz sands with

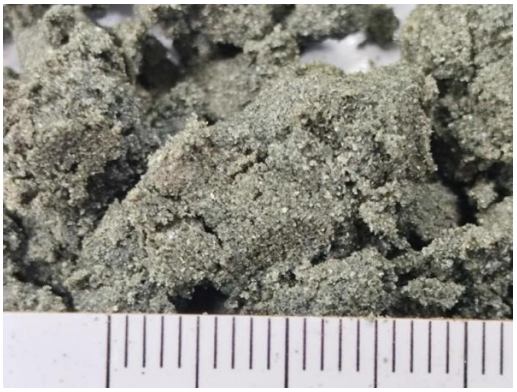


Figure 9. Drilled sediment samples from the Lingshui 36-1 target area

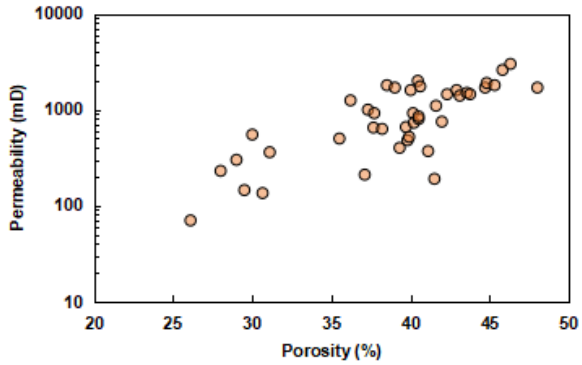


Figure 10. Porosity–permeability relationship of core and cutting-derived reservoir samples from the Lingshui 36-1 target area

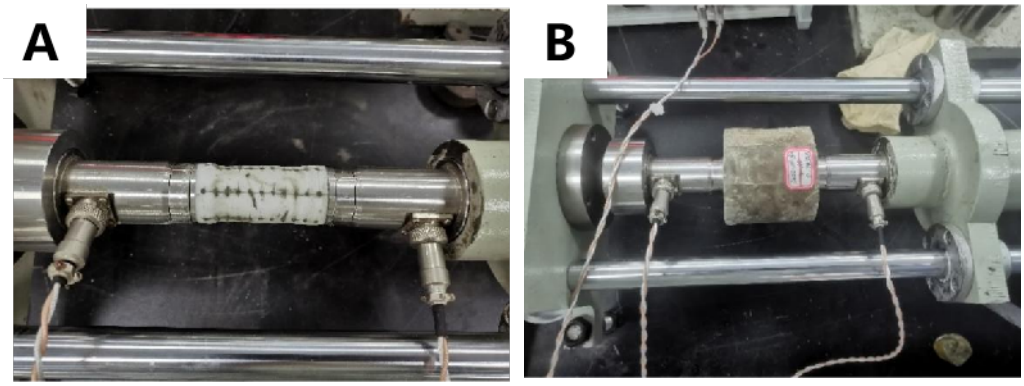


Figure 11. Velocity measurement of recovered samples from the Lingshui 36-1 target area, showing sleeve-packed paste-like sediments and plug-shaped deeper samples. (A) Sleeve-packed paste-like unconsolidated sediment sample. (B) Regular cylindrical core plug sample.

controlled grain sizes were mixed in prescribed proportions and loosely loaded into PTFE sleeves. Dry mass and sleeve volume were used to estimate porosity. P- and S-wave velocities were measured using the transmission method during controlled changes in water saturation or hydrate/free-gas state. No external reservoir-equivalent confining pressure was applied; therefore, the experiments were used solely to identify relative velocity trends and fluid/hydrate sensitivities rather than absolute *in situ* velocities under deep-water pressure. This limitation is critical: effective stress in the laboratory is near zero, whereas *in situ* effective stress at ~300 m below seabed is 1.5–3 MPa. Without a quantitative stress correction (e.g., via the Hertz–Mindlin model), the absolute velocities from these experiments are not physically representative of reservoir conditions.

Table 3 lists the artificial samples used to isolate the effects of porosity, grain size, mineral composition, and

hydrate/free-gas state. Samples 17 (G8) to 20 (G11) were muddy siltstone samples composed of 75% pure quartz sand (grain size: 50 μm) and 25% chlorite. The porosity of the four samples varied significantly (38.80%, 36.12%, 43.63%, and 41.44%, respectively).

Figure 12 shows four free-gas-bearing muddy siltstone samples (G8–G11). In these samples, increasing water saturation replaced compressible gas with water, increasing P- and S-wave velocities. However, in a high-porosity granular framework, the Hertz–Mindlin dry-frame moduli remain low because grain contacts are weak and effective stress is small. Gassmann fluid substitution modifies the pore-fluid contribution but does not eliminate the compliant frame effect. Consequently, P-wave velocity can remain below that of a free water column—including values below 1,500 m/s in the low-stress laboratory measurements. This is a combined frame-fluid response and does not imply that water itself has a lower acoustic velocity. The very low P-wave velocities observed near high water saturation in samples G10 and G11 should therefore be interpreted as relative trend indicators, not as direct pressure-equivalent reservoir values. Under *in situ* conditions, absolute velocities must be recalculated using an effective-stress term constrained by the rock-physics model.

Figure 13 shows that Samples 25 (G13) and 11 (G6) reported similar porosity but different clay content. G13 was a quartz-rich medium sandstone with 500 μm quartz grains, whereas G6 contained 25% chlorite. At comparable water saturation, the clay-rich sample showed lower P- and S-wave velocities, confirming that clay weakens the grain framework and reduces elastic stiffness in the free-gas experimental series.

Figure 14 shows that Samples 4 (G1), 13 (G7), and 24 (G12) were fine- to muddy-fine sandstone analogs with comparable porosity but different mineral composition. Sample 4 (G1) was pure 150 μm quartz sand. Sample 13 (G7) contained 41% 150 μm quartz, 23% sodium feldspar, 26% illite, and 10% calcite. Sample 24 (G12) contained 64%

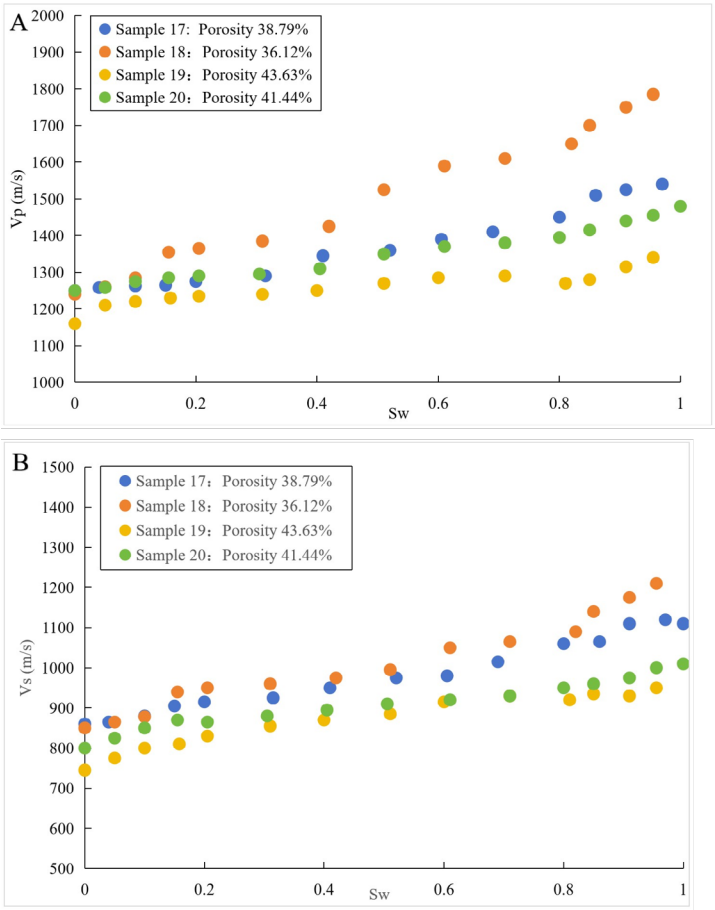


Figure 12. Velocity–water saturation (Sw) relationships for free-gas samples G8–G11. (A) Relationship between P-wave velocity and water saturation. (B) Relationship between S-wave velocity and water saturation.

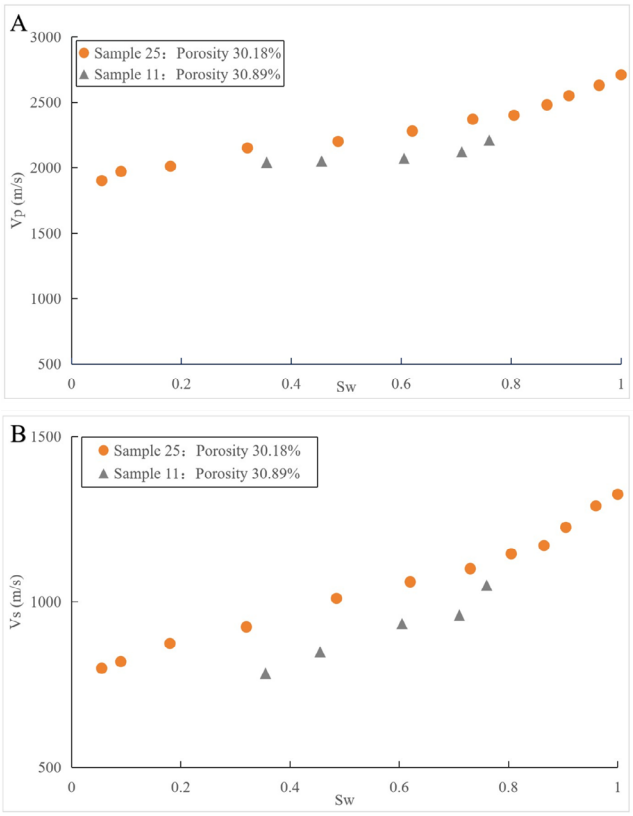


Figure 13. P-wave velocity and S-wave velocity versus water saturation (Sw) for samples with different clay contents (G6 and G13). (A) Relationship between P-wave velocity and water saturation. (B) Relationship between S-wave velocity and water saturation.

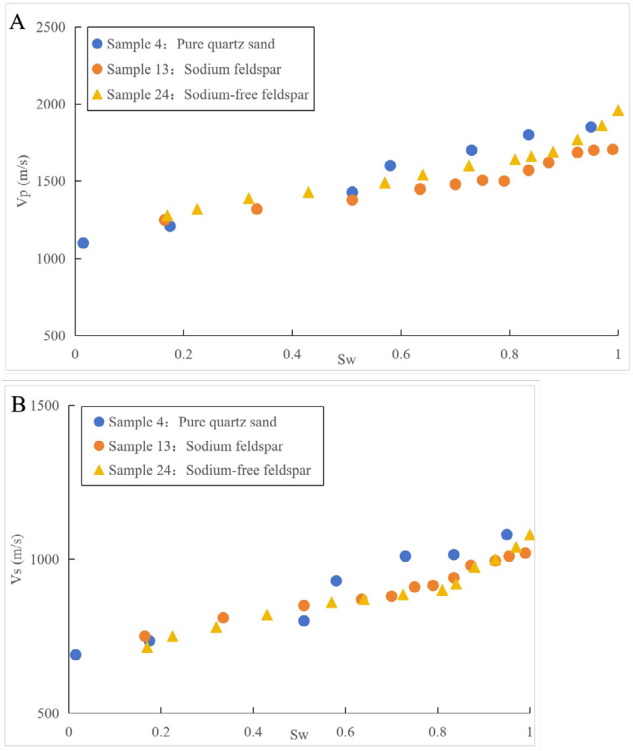


Figure 14. Relationship between velocity and water saturation (Sw) for Samples 4 (G1), 13 (G7), and 24 (G12): (A) P-wave velocity; (B) S-wave velocity

150 μm quartz, 26% illite, and 10% calcite. At comparable saturation, G7 and G12 reported similar velocities because both contained substantial illite, whereas the pure-quartz G1 sample showed slightly higher velocities.

Figure 15 shows that Samples 1 (S1), 3 (S3), 23 (S12), and 2 (S2) were pure-quartz hydrate-bearing analogs with grain sizes of 150, 75, 500, and 1,000 μm, respectively. In this experimental series, decreasing water saturation increased hydrate saturation (higher solid hydrate content). Therefore, P- and S-wave velocities decreased as water saturation increased, which is opposite to the free-gas series. This contrast is physically meaningful and has been clarified to avoid mixing free-gas and hydrate-bearing trends.

Figure 16 shows that Samples 15 (S8), 16 (S9), and 21 (S10) were hydrate-bearing muddy siltstone analogs prepared by adding sodium feldspar, illite, and calcite to 150 μm quartz sand. Their clay and calcite contents were similar, whereas sodium feldspar content varied. The similar velocity–saturation trends among the three samples indicate that, when porosity and clay content are comparable, substituting quartz with feldspar has less influence on elastic velocity than changes in clay content or hydrate saturation.

Figure 17 shows that Samples 9 (S4), 12 (S6), and 22 (S11) were hydrate-bearing medium-grained analogs with similar porosity but different chlorite content. Sample 22 (S11) was pure 500 μm quartz sand; Sample 9 (S4) contained 90% 500 μm quartz and 10% chlorite; and Sample 12 (S6) contained 75% 500 μm quartz and 25% chlorite. Their velocity decreased with increasing water saturation because higher water saturation corresponds to lower hydrate saturation. At comparable saturation, velocity decreased as chlorite content increased.

5.3. Rock-physics crossplot analysis

Rock-physics crossplots from the LS3 well were used to identify the elastic parameters that separate shale, water-bearing, and free-gas-bearing intervals (Figure 18). The panels show well-log classes rather than a direct hydrate classification; hydrate interpretation is constrained separately using the laboratory templates in Figures 15-17 and using the stability analysis. Gas saturation is defined as in **Equation 4** only in free-gas-bearing sediments. Free gas strongly lowered P-wave velocity and impedance, whereas hydrate increased stiffness and velocity when it became part of the load-bearing framework or cement. Consequently, no single monotonic velocity–saturation trend was assumed for all samples. P-wave impedance was used primarily to identify sand-prone reservoirs, whereas the P-wave velocity ratio ranked free-gas-bearing intervals within the reservoir.

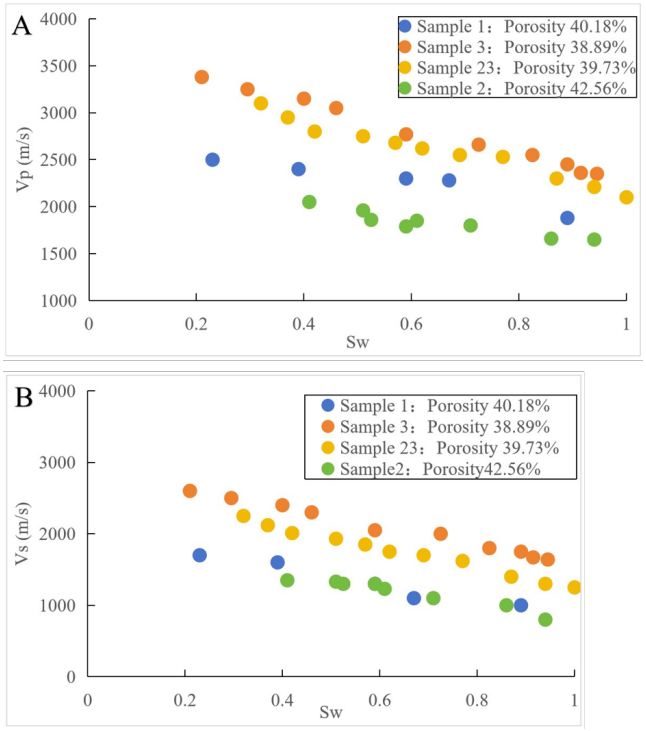


Figure 15. Velocity–water saturation (Sw) relationships for pure-quartz hydrate-bearing samples 1 (S1), 3 (S3), 23 (S12), and 2 (S2): (A) P-wave velocity; (B) S-wave velocity

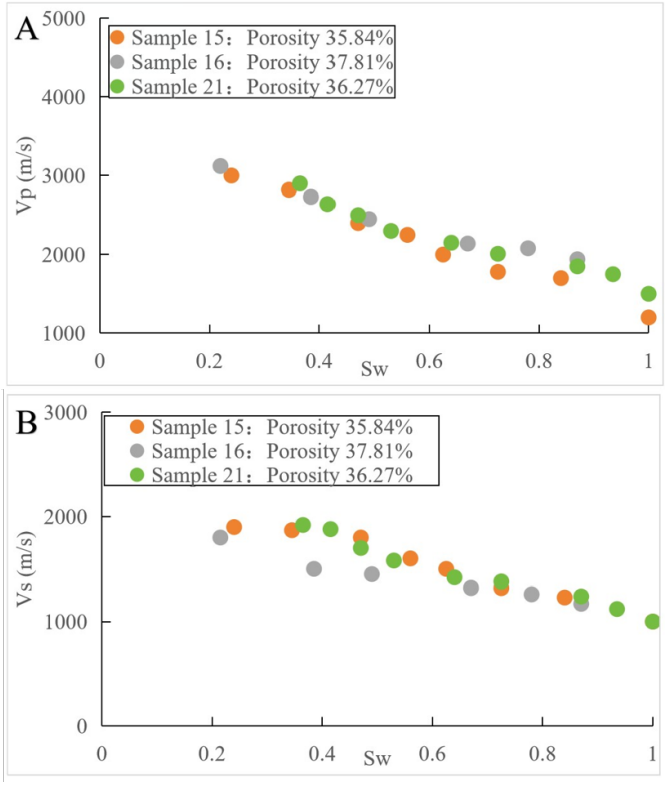


Figure 16. Velocity–water saturation (Sw) relationships for hydrate-bearing Samples 15 (S8), 16 (S9), and 21 (S10): (A) P-wave velocity; (B) S-wave velocity

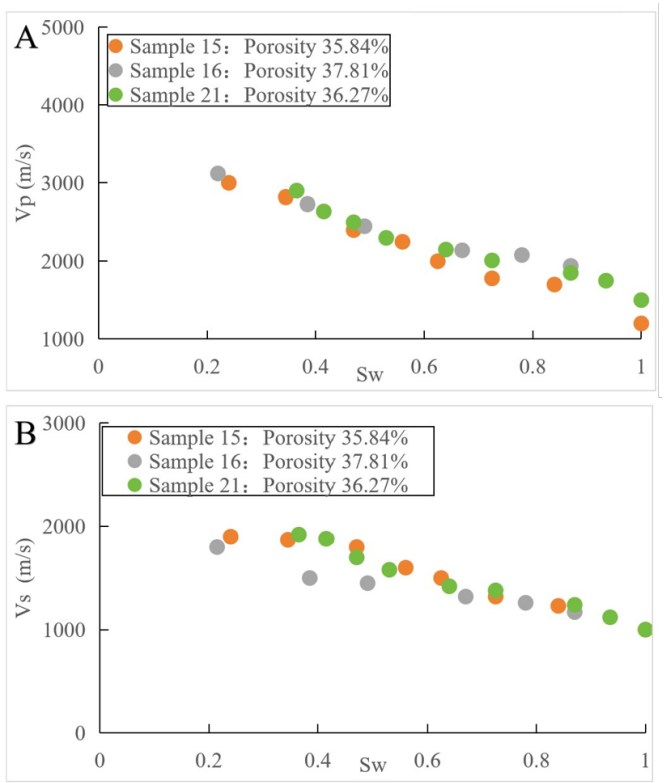


Figure 17. Velocity–water saturation (Sw) relationships for hydrate-bearing Samples 9 (S4), 12 (S6), and 22 (S11): (A) P-wave velocity; (B) S-wave velocity

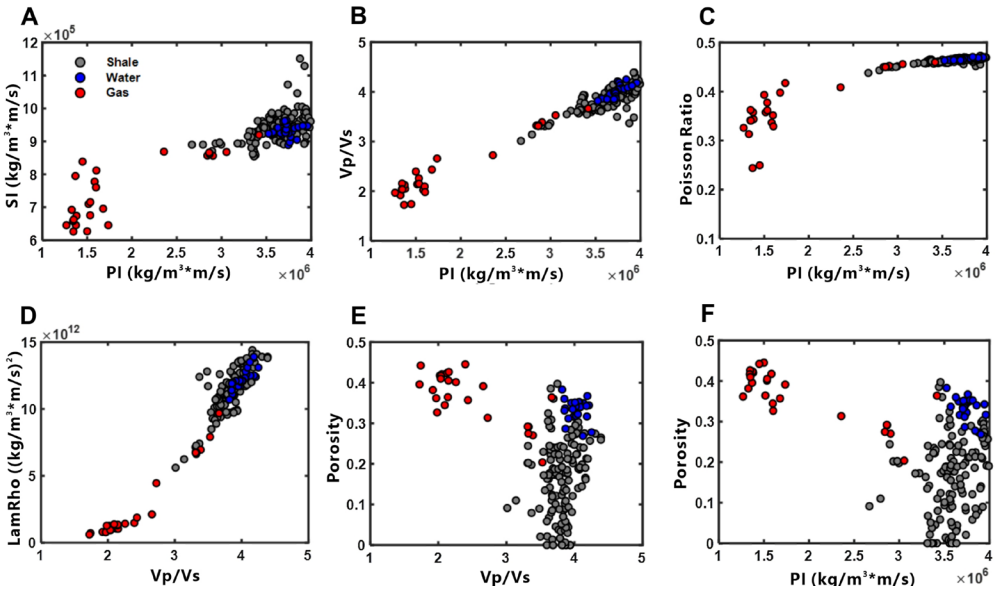


Figure 18. Crossplots of Lingshui 3 (LS3) well-log interpretation from the A2 sand body in the third member of the Ledong Formation: (A) Shear impedance (SI) versus P-wave impedance (PI); (B) P-wave velocity ratio versus PI; (C) Poisson's ratio versus P-wave impedance; (D) Lambda-rho (LamRho) versus P-wave velocity ratio; (E) porosity versus P-wave velocity ratio; (F) porosity versus P-wave impedance. Gray, blue, and red points denote shale, water-bearing, and free-gas-bearing intervals, respectively, based on LS3 well-log interpretation, where shale volume (Vsh) >40% defines shale, water saturation >60% defines water-bearing, and water saturation <40% defines free-gas-bearing intervals.

5.4. Rock-physics modeling strategy

A reproducible rock-physics workflow was established because simple time-average equations are not reliable for undercompacted, high-porosity sediments. Matrix moduli were calculated using Voigt–Reuss-Hill averaging from the XRD mineral proportions. The dry frame at critical porosity was estimated using an enhanced Hertz–Mindlin model; elastic properties below critical porosity were then interpolated with Hashin–Shtrikman bounds, and fluid substitution was performed with the Gassmann equation. The workflow explicitly separates mineral composition, porosity, effective stress, gas/water saturation, and hydrate occurrence.

The Hertz–Mindlin equation was utilized to calculate the bulk modulus K_{HM} and shear modulus G_{HM} of dry rock at critical porosity under weak diagenesis:

$$K_{HM} = \left[\frac{C^2 (1-\Phi_C)^2 G^2}{18\pi^2 (1-v)^2} P \right]^{\frac{1}{3}} \tag{5}$$

$$G_{HM} = \frac{5-4v}{5(2-v)} \left[\frac{3C^2 (1-\phi_C)^2 G^2}{2\pi^2 (1-v)^2} P \right]^{\frac{1}{3}} \tag{6}$$

where C denotes the coordination number, and Φ_C is the critical porosity of the sediment. The term G is the shear modulus of sediment particles, v is the Poisson's ratio of sediment particles, and P is the effective stress between sediment particles. The effective stress of the formation at depth d is as follows:

$$P(d) = \int_0^d \left[\rho_m(h) - \rho_w \right] dh \tag{7}$$

where $\rho_m(h)$ is the formation density at depth h, and ρ_w is the density of seawater.

The parameters used for modeling were C = 8.6, critical porosity φ_c = 0.40, and seawater density ρ_w = 1.03 g/cm^3; mineral moduli were obtained from the Voigt–Reuss–Hill average of quartz, feldspar, carbonate, and clay components. Methane-gas and formation-water moduli and densities were assigned as sensitivity end members, while hydrate-bearing cases were modeled either as solid hydrate stiffening the frame or as hydrate occupying pore space, depending on the interpreted occurrence mode. Model outputs were calibrated to LS36-1 logs and laboratory trends. The values of C = 8.6 and φ_c = 0.40 were chosen as central estimates based on published values for unconsolidated sand. We emphasize that these parameters are not uniquely constrained by the available data. A sensitivity test showed that varying C between 7 and 9 and φ_c between 0.37 and 0.43 changed the predicted P-wave impedance by 8%–12%. This uncertainty is smaller than the impedance contrast between free-gas-bearing and water-bearing sands observed in the LS3 well (25%–30%), supporting the applicability of the current model for first-

order interpretation. However, the uncertainty should be borne in mind when interpreting subtle anomalies near the detection limit.

The model converts geological and laboratory observations into seismic-scale elastic indicators. As shown in Figure 19, the calibrated rock-physics model was used to build a seismic-response template for hydrate-bearing and free-gas-bearing ultra-shallow reservoirs.

5.5. Simulation of seismic reflection characteristics

Forward seismic modeling was performed by assigning P-wave velocity, S-wave velocity, and density from the calibrated rock-physics model and computing angle-dependent reflection coefficients using the exact Zoeppritz equations (Figure 20). The reflection coefficients were convolved with a representative seismic wavelet to generate synthetic seismic records. This procedure avoids relying on small-angle or weak-contrast approximations.

The forward-modeling results show that hydrate-bearing intervals produced high P-wave impedance at their top, where hydrate increased frame stiffness and velocity. In contrast, free-gas-bearing intervals commonly produced low P-wave impedance because even small amounts of gas strongly reduced the P-wave modulus. Hydrate-bearing layers thicker than approximately 3 m were more readily expressed on seismic profiles; thinner layers were affected by tuning and vertical-resolution limits in deep-water seismic data.

Where thin hydrate overlied thicker free gas, the seismic response appeared as a red–black–red event combination.

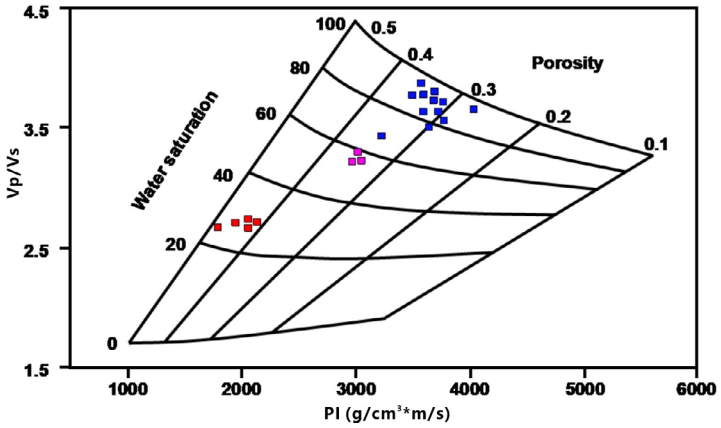


Figure 19. Forward-modeling template for the expected seismic responses of deep-water ultra-shallow hydrate-bearing and free-gas-bearing reservoirs

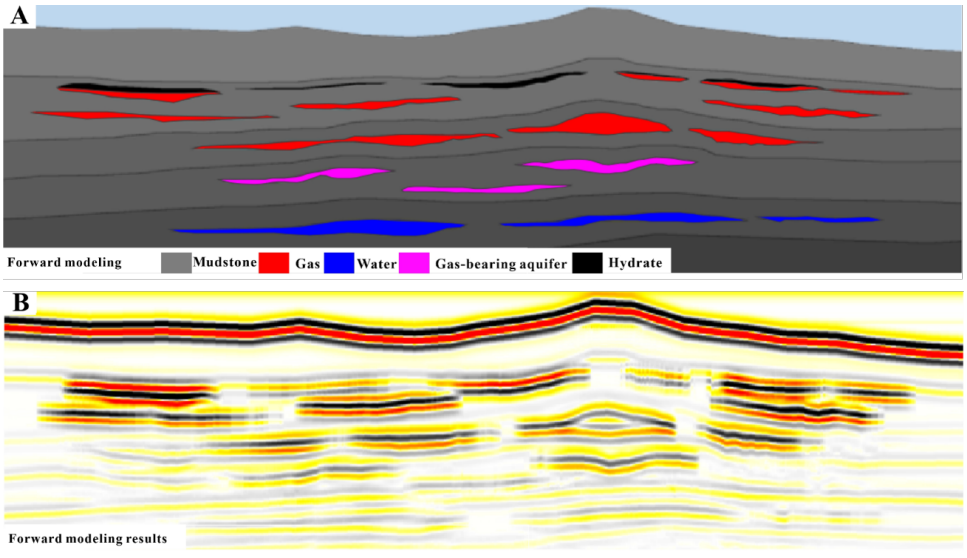


Figure 20. Forward-modeling results for deep-water ultra-shallow hydrate/free-gas reservoir combinations. (A) Layered hydrate/free-gas reservoir model setup. (B) Synthetic seismic reflection responses.

The top hydrate interface was controlled mainly by high impedance, whereas the top free-gas interface was controlled by low impedance. With increasing burial depth and temperature, hydrate thickness decreased, and the free-gas low-impedance response became more prominent. These responses are qualitative templates and must be calibrated locally with well-log and rock-physics constraints.

Gas-bearing water layers and gas layers can be difficult to separate using amplitude alone, especially where reservoir thickness is large or tuning effects are strong. Therefore, the interpretation used a combined indicator set including P-wave impedance, P-wave velocity ratio, porosity, and water/gas saturation rather than a single amplitude attribute.

6. Field application and internal validation

Pre-stack simultaneous inversion was applied to well-controlled seismic data around LS36-1 to obtain P-wave impedance and P-wave velocity ratio volumes (Figure 21). The inversion workflow used well-log calibration, wavelet extraction, low-frequency model construction, and angle-stack inversion. The resulting elastic volumes were interpreted using the rock-physics templates described above. Because no independent blind well was available, validation is limited to consistency with the drilling, logging, and sample data from the same target area.

In the inversion profiles, hydrate/free-gas combinations are expressed using a three-event red–black–red pattern. The upper event corresponds to the top of the hydrate-bearing interval, the middle event approximates the hydrate/free-gas transition or top of the free-gas interval, and the lower event represents the base of the gas-bearing interval. The strength and continuity of these events depend on hydrate thickness, gas saturation, reservoir thickness, and seismic resolution.

Plane-attribute analysis shows that amplitude anomalies, low P-wave impedance, low P-wave velocity ratio, high porosity, and low water saturation overlapped in the most favorable gas-bearing intervals (Figure 22). Because Figure 22B presents the water saturation profile, gas saturation was derived only within the free-gas interpretation as in **Equation 4**. This overlap provides a practical ranking criterion for shallow gas targets, not a direct estimate of reserve size or production capacity; it is an exploration-scale prediction calibrated to available well and sample data.

The interval with the strongest elastic response corresponded to the interpreted thick gas-bearing reservoir. The attenuation of elastic anomalies toward the reservoir margins is consistent with thinning or lateral termination of the sand body. Predicted P-wave impedance, P-wave velocity ratio, porosity, and water saturation agree with LS3 logging interpretation within the available well-control range. Because the same well contributes to model calibration and checking, this agreement demonstrates internal consistency rather than independent blind validation.

7. Discussion

The LS36-1 case illustrates how shallow gas accumulation in ultra-deep-water settings can be evaluated when weakly consolidated reservoirs, hydrate stability, and seismic resolution interact. The main advance is not the description of a single gas discovery, but the integration of submarine-fan reservoir prediction, gas-source constraints, laboratory velocity trends, and rock-physics-guided seismic inversion into one case-calibrated interpretation framework.

The velocity–saturation behavior observed in the experiments emphasizes the need to distinguish free-gas-bearing sediments from hydrate-bearing sediments. In free-gas samples, increasing water saturation replaces a highly compressible gas phase with water, thereby increasing both P- and S-wave velocities under low-stress laboratory conditions. In hydrate-bearing samples, lower water saturation can correspond to higher hydrate saturation; if hydrate contributes to the load-bearing frame or cementation, stiffness and velocity may increase even as water saturation decreases. Treating these two trends as a single monotonic relationship would lead to an incorrect physical interpretation of seismic anomalies.

From an effective medium theory perspective, the Hertz–Mindlin model typically predicts higher dry-frame shear moduli than observed in ambient-pressure laboratory measurements of weakly consolidated sediments, leading to overestimation of the Kdry/Gdry ratio, where Kdry is the dry-rock bulk modulus, and Gdry is the dry-rock shear modulus. For unconsolidated marine sediments, an increase in effective stress from 0 to 3 MPa can increase P-wave velocity by 200–500 m/s or more. All ambient-pressure laboratory velocity measurements in this study (Figures 12–17) therefore reflect only relative trends and cannot be directly extrapolated to *in situ* reservoir conditions without stress correction.

Compared with established hydrate provinces such as the Shenhu area, the Nankai Trough, and the Gulf of Mexico, the LS36-1 system is distinctive because a thermogenic coal-measure gas supply is coupled with Quaternary submarine-fan sand bodies in an ultra-deep-water setting. Mukherjee *et al.*[32] developed a data-driven hydrate-saturation proxy from resistivity and P-wave-velocity increments and tested

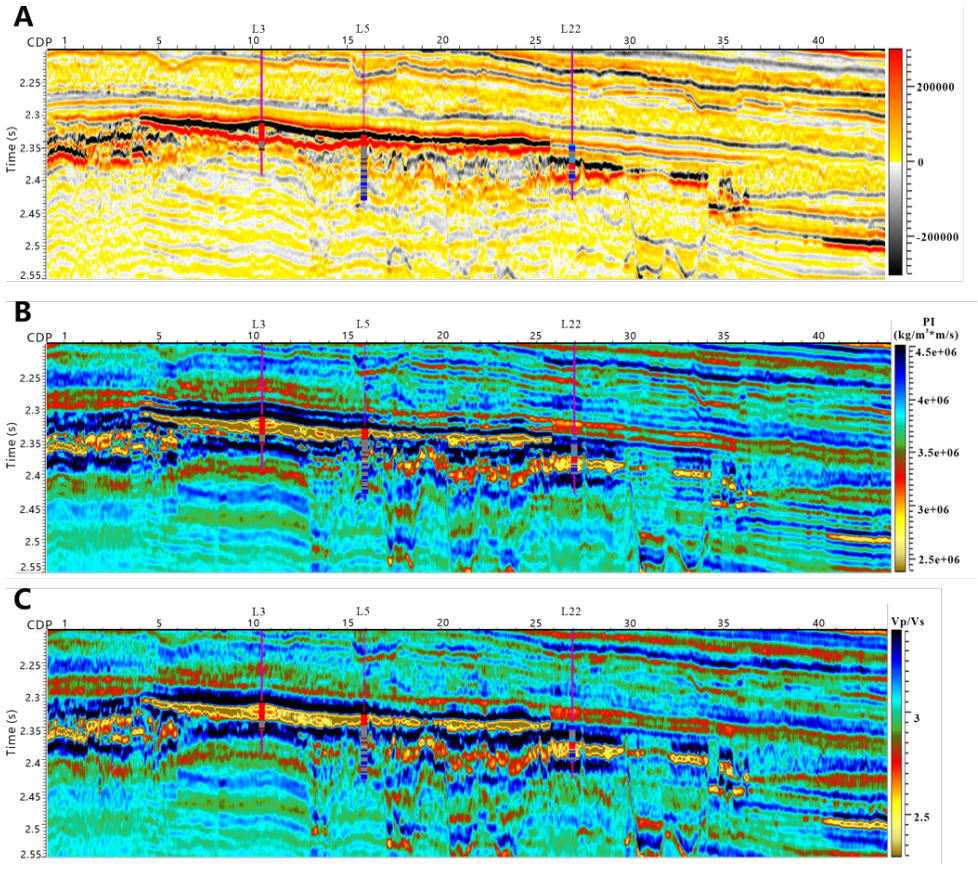


Figure 21. Field inversion results from the Lingshui 36-1 target area: (A) post-stack seismic profile; (B) P-wave impedance inversion profile; (C) P-wave velocity-ratio inversion profile
Abbreviation: CDP: Common depth point.

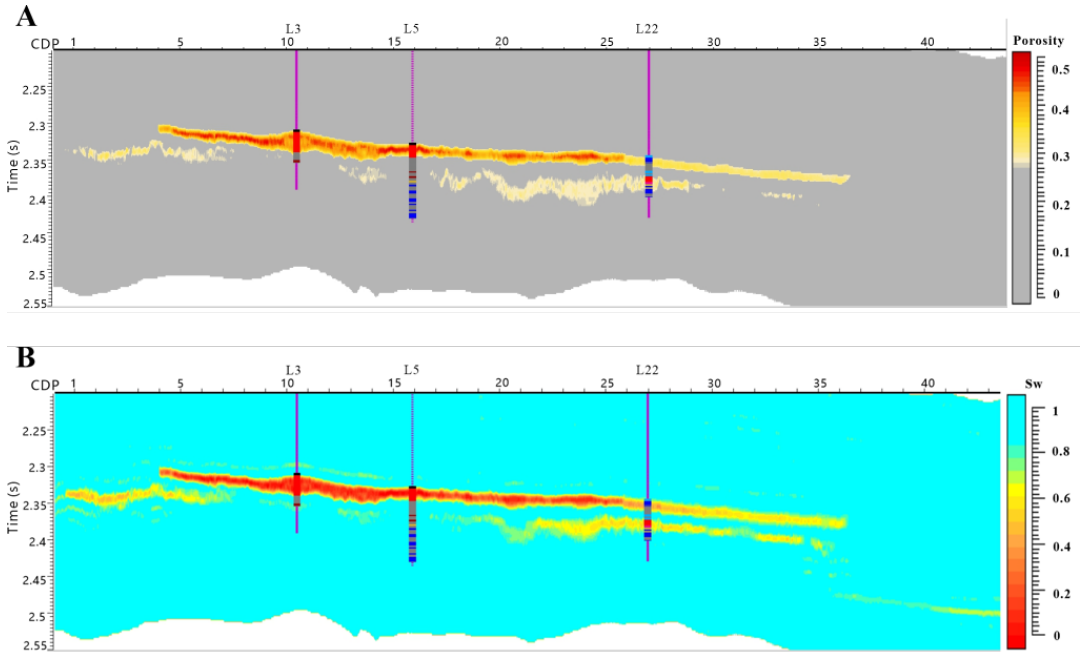


Figure 22. Field prediction results from the Lingshui 36-1 target area: (A) porosity profile; (B) water-saturation (Sw) profile
Abbreviation: CDP: Common depth point.

it across four wells in the Krishna–Godavari offshore basin. That study demonstrates the value of multiwell log calibration, whereas the present LS36-1 interpretation uses a rock-physics template and one principal well, therefore making a weaker, case-specific claim. The two approaches are complementary rather than directly interchangeable. In LS36-1, low P-wave impedance may indicate sand-prone free-gas intervals, whereas relatively high impedance near the hydrate stability zone may reflect hydrate stiffening rather than a conventional compacted sandstone response. The interpretation therefore depends on joint evaluation of stratigraphic position, seismic facies, impedance, velocity ratio, and gas-source evidence.

Several uncertainties remain. First, the laboratory measurements were made on recovered or artificial samples without reservoir-equivalent confining pressure, so the absolute velocities should not be transferred directly to *in situ* conditions. Second, the inversion is calibrated mainly with one principal well; the results demonstrate internal consistency but not independent blind-well validation. Third, hydrate stability depends on laterally variable heat flow, seabed temperature, pressure, and gas composition. Fourth, the P-wave impedance-to-porosity and Vp/Vs-to-saturation conversions inherit LS3 calibration uncertainty and should not be interpreted as independent measurements. These factors require uncertainty-aware interpretation of the predicted porosity and water-saturation profiles.

The workflow is therefore best regarded as a practical, case-specific interpretation scheme for ranking shallow gas targets in the LS36-1 area. Future work should test the same rock-physics template against additional wells, pressure–temperature-preserved samples and independent seismic volumes before transferring it to other deep-water submarine-fan systems.

8. Conclusion

The proposed workflow is best regarded as a practical, case-specific interpretation scheme for ranking shallow gas targets in the LS36-1 area. Future work should test the same rock-physics template against additional wells, pressure-temperature-preserved samples, and independent seismic volumes before transferring it to other deep-water submarine-fan systems.

Due to the ambient-pressure nature of the laboratory experiments and the single-well calibration, the inverted P-wave impedance and porosity values carry significant systematic uncertainty. These predictions should therefore be used for relative target ranking.

Acknowledgments

None.

Funding

The study was funded by the Science and Technology Special Fund of Hainan Province (ZDYF2024GXJS031).

Conflict of interest

All authors are employees of CNOOC Hainan Branch; however, they were not involved in any activities that could constitute a conflict of interest in relation to this study.

Author contributions

Conceptualization: Jianxiang Pei
Investigation: Chongyan Wu
Methodology: Fang Li, Wanyuan Sun
Formal analysis: Yanhua Xie
Writing–original draft: Jinpeng Li
Writing–review & editing: Jinpeng Li

Availability of data

All data analyzed are presented in the paper.

References

1. Waite WF, Santamarina JC, Cortes DD, *et al*. Physical properties of hydrate-bearing sediments. *Rev Geophys*. 2009;47(4):RG4003.

   doi: 10.1029/2008rg000279

2. Sloan ED Jr, Koh CA. *Clathrate Hydrates of Natural Gases*. 3rd ed. Boca Raton, FL: CRC Press; 2007.

   doi: 10.1201/9781420008494

3. Collett TS. Natural Gas Hydrates of the Prudhoe Bay and Kuparuk River Area, North Slope, Alaska. *AAPG Bull*. 1993;77(5):793-812.

   doi: 10.1306/bdff8d62-1718-11d7-8645000102c1865d

4. Kvenvolden KA. Gas hydrates—geological perspective and global change. *Rev Geophys*. 1993;31(2):173-187.

   doi: 10.1029/93rg00268

5. Avseth P, Mukerji T, Mavko G. *Quantitative seismic interpretation: Applying rock physics tools to reduce interpretation risk*. Cambridge, UK: Cambridge University Press; 2005.

   doi: 10.1017/CBO9780511600074

6. Shi HS, Yang JH, Zhang YZ, Gan J, Yang JH. Qiongdongnan Pendi Dizhi Renshi Chuangxin yu Shenshui Lingyu Tianranqi Kantan Zhongda Tupo [Geological understanding innovation and major breakthrough in natural gas exploration in deep-water in Qiongdongnan Basin]. *China Pet Explor*. 2019;24(6):691-698. [In Chinese]

   doi: 10.3969/j.issn.1672-7703.2019.06.001

7. Huang H, Huang B, Huang Y, Li X, Tian H. Condensate

origin and hydrocarbon accumulation mechanism of the deepwater giant gas field in western South China Sea: A case study of Lingshui 17-2 gas field in Qiongdongnan Basin. *Pet Explor Dev*. 2017;44(3):409-417.

doi: 10.1016/S1876-3804(17)30047-2

8. Yu GM, Gu CW, Song Y, *et al*. Shenshui Qiancengqi Zuanjing Fengxian Pinggu yu Kongzhi Jishu [Risk assessment and control technology for deep-water shallow-gas drilling]. *Oil Drilling & Production Technology*. 2022;44(3):297-301. [In Chinese]

doi: 10.13639/j.odpt.2022.03.005

9. Li P, Du J, Liu LJ, Cao CX, Xu YQ. Woguo Jinhai Haidi Qiancengqi Fenbu Tezheng [Distribution characteristics of the shallow gas in Chinese offshore seabed]. *Chin J Geol Hazard Control*. 2010;21(1):69-74. [In Chinese]

doi: 10.3969/j.issn.1003-8035.2010.01.015

10. Gao Y, Jin Q, Zhu G. Genetic types and distribution of shallow-buried natural gases. *Pet Sci*. 2010;7(3):347-354.

doi: 10.1007/s12182-010-0076-y

11. Li SK, Wen XT, Ruan YQ, Li T, Zhang R, Zhang JM. Jiyu White Moxing de Hanqi Shayyan Chuizhi Rushe Dizhen Xiangying Tezheng Fenxi [Analysis of seismic response characteristics from vertical incident in sandstone gas reservoir based on the White model]. *Geophysical Prospecting for Petroleum*. 2017;56(2):232-239. [In Chinese]

doi: 10.3969/j.issn.1000-1441.2017.02.010

12. Deng JX, Han DH, Wang S. Yingli Songsong dui Keli Wuzhi Tanxing Xingzhi de Yingxiang ji Dengxiao Jiezhi Moxing Jiaozheng Yanjiu [A study of the influence of stress relaxation on the elastic properties of granular materials and the calibration of effective media model]. *Chin J Geophys*. 2011;54(4):1079-1089. [In Chinese]

doi: 10.3969/j.issn.0001-5733.2011.04.023

13. Chong ZR, Yang SHB, Babu P, Linga P, Li XS. Review of natural gas hydrates as an energy resource: Prospects and challenges. *Appl Energ*. 2016;162:1633-1652.

doi: 10.1016/j.apenergy.2014.12.061

14. Zhang W, Liang J, Su P, *et al*. Distribution and characteristics of mud diapirs, gas chimneys, and bottom simulating reflectors associated with hydrocarbon migration and gas hydrate accumulation in the Qiongdongnan Basin, northern slope of the South China Sea. *Geol J*. 2018;54(6):3556-3573.

doi: 10.1002/gj.3351

15. Liu T, Bao X, Zhu X, Li A. Han Tianranqi Shuihewu Chuceng Shuaijian Yanshi Wuli Yanjiu Jinzhan [Review of rock-physics studies on natural gas hydrate-bearing sediment attenuation]. *Rev Geophys and Planetary Physics*. 2024;55(3):369-380. [In Chinese]

doi: 10.19975/j.dqyxx.2023-028

16. Yuan H, Han Dh, Wang Y. A review of rock physical models for elastic properties characterization of gas hydrate bearing sediments. *J Pet Sci Eng*. 2022;218:111013.

doi: 10.1016/j.petrol.2022.111013

17. Wang XJ, Han L, Liu JZ, Jin JP, Kuang ZG, Zhou JL. Tianranqi Shuihewu yu Youliqi Gongcun de Diqiu Wuli Tezheng yu Shibie [Geophysical characteristics and identification of the coexistence of gas hydrate and free gas]. *Earth Sci Front*. 2025;32(2):20-35. [In Chinese]

doi: 10.13745/j.esf.sf.2024.11.22

18. Jia PW, Lu Y, Su PB, *et al*. Shenhu Haiyu Tianranqi Shuihewu Cejing-Dizhen Xiangying Tezheng [Logging and seismic response characteristics of natural gas hydrate in the Shenhu area]. *Acta Geologica Sinica*. 2024;98(9):2654-2665. [In Chinese]

doi: 10.19762/j.cnki.dizhixuebao.2024312

19. Lai H F, Qiu H J, Liang J Q, *et al*. Geochemical Characteristics and Gas-to-Gas Correlation of Two Leakage-type Gas Hydrate Accumulations in the Western Qiongdongnan Basin, South China Sea. *Acta Geologica Sinica (Eng)*. 2022;96(2):680-690.

doi: 10.1111/1755-6724.14931

20. Zhan L, Liu B, Zhang Y, Lu H. Rock Physics Modeling of Acoustic Properties in Gas Hydrate-Bearing Sediment. *J Mar Sci Eng*. 2022;10(8):1076.

doi: 10.3390/jmse10081076

21. Ghosh R, Ojha M, Kumar P. Review of rock physics theories for quantifying gas hydrate and associated uncertainties. *J Asian Earth Sci*. 2023;256:105828.

doi: 10.1016/j.jseaes.2023.105828

22. Wang X, Zhou J, Li S, *et al*. Constraints on Characteristics and Distribution of Gas Hydrate and Free Gas Using Broad-Band Processing of Three-Dimensional Seismic Data. *J Ocean Univ China*. 2024;23(5):1233-1247.

doi: 10.1007/s11802-024-5980-7

23. Wang X, Collett TS, Lee MW, Yang S, Guo Y, Wu S. Geological controls on the occurrence of gas hydrate from core, downhole log, and seismic data in the Shenhu area, South China Sea. *Mar Geol*. 2014;357:272-292.

doi: 10.1016/j.margeo.2014.09.040

24. Wu S, Zhang G, Huang Y, Liang J, Wong HK. Gas hydrate occurrence on the continental slope of the northern South China Sea. *Mar Pet Geol*. 2005;22(3):403-412.

doi: 10.1016/j.marpetgeo.2004.11.006

25. Chen LT, Pei JX, Xu FH, *et al*. Qiongdongnan Pendi Lingshui 36-A Qu Chaoqianceng Tianranqi Guanjian Chengcang Tiaojian yu Chengcang Moshi [Key accumulation conditions and accumulation model of ultra-shallow gas in the Lingshui 36-A area, Qiongdongnan Basin]. *Pet Geol Exp*.

2026;48(2):418-432. [In Chinese]

doi: 10.11781/sysydz2026020418

26. Huang SZ, Li F, Song P, Hu B, Sun WY. Qiongdongnan Pendi Chaoshenshui Qianbu Qicang Diqiu Wuli Shibie Jishu [Geophysical identification technology for ultra-deep water shallow gas reservoirs in the Qiongdongnan Basin]. *Earth Sci*. 2024;49(1):313-323. [In Chinese]

doi: 10.3799/dqkx.2022.339

27. Zhang GC, Ji M, Chen Y, Gan J, Wang DD, Zhang CY. Qiongdongnan Pendi "Qi Juji Dai" de Chengcang Tezheng yu Kantan Qianli [Accumulation characteristics and exploration potential of the "gas accumulation belt" in the Qiongdongnan Basin]. *Acta Petrolei Sinica*. 2024;45(1):226-240. [In Chinese]

doi: 10.7623/syxb202401013

28. Wang Z. Fundamentals of seismic rock physics. *Geophysics*. 2001;66(2):398-412.

doi: 10.1190/1.1444931

29. Ren JF, Chen YH, Xu MJ, *et al*. Nanhai Beibu Qiongdongnan Pendi Shazhi Tianranqi Shuihewu Chuceng Chenji Tezheng ji Chengcang Moshi [Sedimentary characteristics and accumulation model of sandy gas hydrate reservoirs in the Qiongdongnan Basin, northern South China Sea]. *Earth Sci Front*. 2025;32(2):94-112. [In Chinese]

doi: 10.13745/j.esf.sf.2024.6.52

30. Xu C, Wu K, Pei J, Hu L. Enrichment mechanisms and accumulation model of ultra-deep water and ultra-shallow gas: A case study of Lingshui 36-1 gas field in Qiongdongnan Basin, South China Sea. *Pet Explor Dev*. 2025;52(1):50-63.

doi: 10.1016/s1876-3804(25)60004-8

31. Chen ZG, Jiang T, Kuang ZG, Cheng C, Xiong PF, Chen Y. Qiongdongnan Pendi Tianranqi Shuihewu yu Qiancengqi Gongsheng Tixi Chengcang Tezheng [Accumulation characteristics of the coexistence system of gas hydrate and shallow gas in the Qiongdongnan Basin]. *Earth Science*. 2022;47(5):1619-1634. [In Chinese]

doi: 10.3799/dqkx.2022.094

32. Mukherjee B, Sain K, Ghosh R, Konar S. Translation of machine learning approaches into gas hydrate saturation proxy: a case study from Krishna-Godavari (KG) offshore basin. *Mar Geophys Res*. 2024;45(2):12.

doi: 10.1007/s11001-024-09546-3